Nanoscale

PAPER

View Article Online
View Journal



Cite this: DOI: 10.1039/d5nr02667a

# Surface-engineered gold nanorods for targeted delivery of PD-L1 siRNA and cancer chemo-phototherapy

Lilia Arellano, [a] Eva Villar-Álvarez, [a] Adriana Cambón, [a] Alba Costa-Santos, [a] Óscar Abelenda, [a] Alberto Pardo, *[a] Antonio Topete, *[a,b] Silvia Barbosa [a] and Pablo Taboada [a]

Nowadays, cancer remains a global leading cause of death, with therapeutic advances often hindered by drug resistance and adverse side effects. The integration of nanotechnology with immunotherapy has emerged as a promising approach to enhance specificity and efficacy of oncological treatments. A key immunotherapeutic target is the so-called programmed death-ligand 1 (PD-L1), a protein that enables tumors to evade immune surveillance and increase their chemotherapy resistance. Interestingly, RNA interference using small interfering RNA (siRNA) targeting PD-L1, has shown potential in reactivating anti-cancer immune responses. However, efficient delivery of siRNA still faces challenges in terms of stability, cellular uptake, and/or targeted release. In this study, we developed a multifunctional theranostic nano-platform based on gold nanorods (GNRs) surface-engineered through a layer-by-layer assembly with poly (styrene sulfonate), poly(L-lysine), and hyaluronic acid, to provide enhanced stability and active targeting towards CD44 receptors overexpressed in cancer cells. Within the polymeric multilayers PD-L1 siRNA, doxorubicin and indocyanine green were loaded for multimodal therapeutic activity. The anti-tumor effect, siRNA transfection efficiency and cell death mechanism of the nanoplatform was evaluated on HeLa cells expressing PD-L1 and CD44 and Balb/3T3 fibroblasts. The surface-engineered GNRs-based nanosystem efficiently transfected PD-L1 siRNA and allowed subsequent application of multimodal chemo-, photodynamic and photothermal therapy with enhanced cytotoxicity.

Received 10th July 2025,
Accepted 8th October 2025
DOI: 10.1039/d5nr02667a
rsc.li/nanoscale



## 1. Introduction

Cancer is one of the major societal, public health, and economic hurdles nowadays, being the cause of nearly one-quarter of all deaths due to noncommunicable diseases worldwide.[1] Although significant advancements in the treatment of various types of cancer have been achieved in recent years, the effectiveness of current therapies remains limited by drug resistance and adverse side effects.[2,3] In this context, the combination of nanotechnology with immunotherapy has emerged as a promising approach to enhance the specificity and efficacy of oncological treatments.[4]

Immunotherapy has revolutionized cancer treatment by leveraging the patient's own immune system to target and eliminate tumor cells.[5] However, tumors possess several mechanisms to evade the immune system, including the expression of PD-L1, which is one of the most relevant immunological checkpoints.[6] PD-L1 interacts with the programmed death 1 (PD-1) receptor on T cells, thereby inhibiting their activity and allowing cancer cells to escape immune surveillance.[7] Furthermore, the overexpression of PD-L1 in cancer cells has several significant effects beyond facilitating immune escape. First, it promotes cellular proliferation and accelerates tumor growth rate by enhancing glucose metabolism and fatty acid oxidation.[8] Moreover, PD-L1 overexpression has been also associated with increased survival, growth, and migration ability of cancer cells, along with increased resistance to chemotherapy-based treatments.[9–11] Therefore, the controlled inhibition of PD-L1 constitutes a promising strategy to enhance the efficacy of the antitumor responses of the immune system and improve the effectiveness of cancer therapies.

On the other hand, gene therapies involve the manipulation of the genome and/or the modulation of transcriptional–translational processes to selectively inhibit, knockdown, or activate

[a]Colloids and Polymers Physics Group, Particle Physics Department, Institute of Materials (iMATUS), and Health Research Institute (IDIS), University of Santiago de Compostela, 15782 Santiago de Compostela, Spain.
E-mail: alberto.pardo.montero@usc.es, antonio.topete.camacho@usc.es
[b]Immunology Laboratory, Department of Physiology, University Center for Health Sciences (CUCS), University of Guadalajara, 44340 Guadalajara, Mexico

specific genes associated with a particular disease.[12] Amongst gene therapies, small interfering RNA (siRNA) has emerged as a powerful biotechnological tool for silencing the expression of specific genes by cleaving its complementary messenger RNA (mRNA), thus hindering their translation into protein.[13] Interestingly, recent works have evaluated the use of siRNA molecules to inhibit the overexpression of PD-L1 in cancer cells.[14] Different nanocarriers, including poly(lactic-*co*-glycolic acid) (PLGA) nanoparticles (NPs),[15] nucleic acid-based nanogels,[16] and poly(ethyleneimine)-lipid NPs,[17] have been explored for the delivery of PD-L1-targeted siRNA to reactivate antitumor immune responses.

Nonetheless, to be considered as a reliable therapeutic option, siRNA-loaded nanostructures must overcome several challenges, including their typical poor biostability and biodistribution, low cellular uptake, rapid degradation by nucleases, and the potential to trigger non-specific immunogenic reactions.[18] Therefore, the development of novel delivery systems that can effectively transport, protect, and release siRNA remains an important challenge. In this context, the design of carrier nanoplatforms based on gold nanorods (GNRs) constitutes an interesting and still underexplored alternative for the encapsulation, transport, and controlled delivery of genetic material.[19] In addition to the high stability, easy functionalization, and excellent biocompatibility of gold-based nanostructures, GNRs display outstanding optical properties and high photothermal capability, which enable their use as plasmonic photothermal therapy (PTT) agents.[20]

In this work, we have developed a theranostic nanosystem based on GNRs functionalized with poly(styrene sulfonate) (PSS) and poly(L-lysine) (PLL) using a layer-by-layer methodology. These polymers provide colloidal stability to the nanoplatform after the removal of the potentially toxic cetyltrimethylammonium bromide (CTAB) molecules used during the synthesis of GNRs. In order to increase the anticancer therapeutic effect of the nanoplatform, doxorubicin (DOXO), the biosafe photosensitizer indocyanine green (ICG) and PD-L1 siRNA oligonucleotide were integrated within the polyelectrolyte multilayers adsorbed on GNRs. Finally, a hyaluronic acid (HA) layer was added onto the surface of the hybrid nanostructures, thus increasing their stability and providing them with active targeting to CD44 receptor, which is overexpressed in different types of cancer cells.[21–23]

In this way, we have designed a multitherapeutic, CD44-targeted, and photoresponsive nanoplatform, GNR/PSS/DOXO/PLL@ICG/siRNA/HA, abbreviated as GNR-DIsH, which enables the on-demand release of bioactive compounds through near-infrared (NIR) stimulation of GNRs and enzymatic degradation of PLL. The silencing activity of PD-L1 siRNA, as well as the combined and isolated therapeutic effects of PTT and photodynamic therapy (PDT), were evaluated in HeLa cells, a PD-L1-expressing and CD44-overexpressing tumoral cell line,[24–27] and in Balb/3T3 murine fibroblasts, which have low CD44 expression and express a mouse PD-L1 that is not degraded by the human PD-L1 siRNA.[28] The cell death mechanism induced by the multimodal therapy using GNR-DIsH was also assessed.

# 2. Materials and methods

## 2.1. Materials

Cetyltrimethylammonium bromide (CTAB) for molecular biology, tetrachloroauric acid trihydrate ($HAuCl_4 \cdot 3H_2O$), silver nitrate ($AgNO_3$), sodium borohydride ($NaBH_4$), poly(sodium-4-styrenesulfonate) (PSS; $M_w \sim 70$ kDa), poly-L-lysine hydrobromide (PLL; $M_w \sim 22$ kDa), hyaluronic acid (HA; $M_w \sim 15$ kDa) and fluorometric intracellular ROS kit were purchased from Sigma-Aldrich. Ascorbic acid, sulfo-*N*-hydroxysuccinimide-ICG ester (sulfo-NHS-ICG), and doxorubicin hydrochloride (DOXO·HCl) were purchased from Fluka, Flamma® Fluors, and MedChemExpress, respectively. PD-L1 siRNA and BLOCK-iT™ Fluorescent Oligo, a fluorescein isothiocyanate-labeled siRNA oligomer (siRNA-FITC), with the same length, electric charge, and structure as standard siRNA, were supplied by Sigma-Aldrich and Thermo Scientific, respectively. Heat-inactivated fetal bovine serum (FBS), trypsin-EDTA (0.25×) and PBS pH 7.4 (10×) were purchased from Hyclone, while ProLong Gold Antifade reagent with DAPI and the Cell Death Annexin V-Propidium Iodide kit were supplied by Molecular Probes, and Gerbu Biotechnik, respectively. Cell counting kit-8 (CCK-8) was supplied by Dojindo. All chemicals were used as received. Nuclease-free water was used in all the assays involving siRNA.

## 2.2. Synthesis and characterization of GNRs

GNRs were synthesized following a previously reported seeded-growth method,[29] which is based on the method developed by Nikoobakht *et al.*[30] The experimental details can be found in section S1 of the SI. The UV–visible extinction spectra, and the size and morphology of the obtained nanostructures were measured using a Cary Bio 100 UV–vis spectrophotometer (Agilent Technologies) and a JEM 1011 (JEOL) transmission electron microscope. Fluorescence measurements were carried out using a Cary Eclipse Bio fluorimeter (Agilent Technologies). Measurements of fluorescent molecules in cells were conducted using a FLUOstar OMEGA plate reader (BMG Labtech). Hydrodynamic diameter ($D_H$) and ζ-potential were measured using a Zetasizer Nano ZS (Malvern Instruments). The concentration of GNRs was quantified by means of inductively coupled plasma mass spectroscopy (ICP-MS, Agilent 7700x, Agilent Technologies).

## 2.3. Layer-by-layer coating and loading of bioactive compounds in GNRs

The cationic polyelectrolyte PLL was derivatized with the NIR photosensitizer ICG to generate a PLL@ICG complex by means of an amidation reaction. For full details refer to section S2 of the SI. Afterwards, GNRs were surface-coated with polyelectrolytes and loaded with the bioactive compounds following a previously reported layer-by-layer methodology with minor modifications.[29] Briefly, GNRs were mixed and stirred with solutions of PSS, DOXO, PLL@ICG, PD-L1 siRNA and, finally, with HA to obtain the full nanoplatform, GNR-DIsH, with multitherapeutic and active targeting functionalities. The full

 

details of the layer-by-layer surface modification method are available in section S3 of the SI.

### 2.4. Photoactivation of nanoplatforms with an NIR laser

Functional assays involving light stimulation were conducted using a continuous-wave diode laser source coupled to an optical fiber at a wavelength of 808 nm (Oclaro, Inc.). The diameter of the laser spot was measured with a laser beam profiler (LBP-1-USB, Newport) and was set at 1 cm. A light power meter (Optical Power Meter model 1916c, Newport) was used to calibrate the output power.

### 2.5. Entrapment efficiency and drug loading capacity

The entrapment efficiency (EE%) and drug loading capacity (DL%) of DOXO and PLL@ICG were determined by an indirect method. Briefly, after the polyelectrolyte coating and drug loading process, any DOXO and PLL@ICG unadsorbed on the nanoplatforms and remaining in the supernatants were quantified by UV-vis and fluorescence spectroscopy techniques, respectively. Calibration curves were prepared (Fig. S1A and B), and the amounts of unadsorbed DOXO ($\lambda_{max}$ = 488 nm) or PLL@ICG ($\lambda_{ex}$ = 785 nm, $\lambda_{em}$ = 810 nm) were determined based on the Lambert–Beer law and the linear relationship between fluorescence intensity and concentration observed at low analyte concentrations. The EE% and DL% were calculated using the following equations:

$$EE\% = \frac{drug_{total} - drug_{sup}}{drug_{total}} \times 100 \quad (1)$$

$$DL\% = \frac{drug_{total} - drug_{sup}}{nanoplatform_{total}} \times 100 \quad (2)$$

where $drug_{total}$ and $drug_{sup}$ represent the initial concentration of DOXO or PLL@ICG added during the synthetic process and their concentration in the supernatant after centrifugation, respectively, and $nanoplatform_{total}$ corresponds to the total weight of the nanoplatform after the successive functionalization/loading steps.

To determine the EE% of siRNA within the GNR-DIsH nanoplatforms, they were centrifuged at 9520 × *g* at 20 °C for 20 min, and the siRNA content in the supernatant was determined using the microRNA Qubit fluorescence kit (Invitrogen) by means of a calibration curve (Fig. S1C) following the manufacturer's instructions.

### 2.6. Colloidal stability and release kinetics

The colloidal stability of the nanoplatforms was assessed at pH 3.0, 5.0, 7.4, 9.0 and under different biologically relevant conditions. The cumulative drug release profiles of DOXO, PLL@ICG, and siRNA were measured at 37 °C under 300 rpm magnetic stirring. The release was performed in PBS supplemented with 10% FBS, at pH values of 7.4 and 5.0, in the absence and presence of EDTA-trypsin (50 μL per 40 mL of buffer solution, 3.125 mg $L^{-1}$) and/or NIR irradiation at 1.0 and 2.0 W $cm^{-2}$ for 5 min. The full experimental details can be found in section S4 of the SI.

### 2.7. Cytotoxicity and cellular uptake of nanoplatforms

Cell culture was carried out in an incubator under 5% $CO_2$ at 37 °C and saturating humidity. The complete medium consisted of DMEM supplemented with 10% (v/v) FBS, 0.1 mM non-essential amino acids, 2 mM L-glutamine, 1 mM sodium pyruvate, and 1% penicillin–streptomycin. The cytotoxicity of the GNR-DIsH nanoplatforms was evaluated using the CCK-8 cell proliferation assay kit. For this, cells were seeded in 96-well plates (100 μL, 1.5 × $10^4$ cells per well) and cultured for 24 h under standard conditions. Subsequently, GNR-DIsH at a concentration of 2.5 × $10^{10}$ NPs per mL in culture medium was added to the wells and incubated for 24 and 48 h. Free DOXO, free ICG and Lipofectamine2000™ + siRNA – each at the same concentration as its counterpart encapsulated in GNR-DIsH – were used as positive controls. Negative controls included cells without any treatment and those treated with nanoplatforms without DOXO, PLL@ICG, or siRNA (GNR-H). The absorbance of the samples was measured at 450 nm with a microplate reader (689 Microplate Reader, Bio-Rad). Cell viability was calculated using:

$$\%\,\text{cell viability} = \frac{Abs_{\text{treated cells}}}{Abs_{control}} \times 100 \quad (3)$$

where $Abs_{\text{treated cells}}$ is the absorbance at 450 nm of the treated cells, and $Abs_{control}$ is the absorbance corresponding to the negative controls. The cellular internalization of GNR-DIsH prepared with siRNA-FITC was visualized by TEM and fluorescence microscopy with $\lambda_{ex/em}$ = 585/624 nm for DOXO and $\lambda_{ex/em}$ = 488/520 nm for FITC. For full details of the experimental setup and conditions, refer to section S5 of the SI.

### 2.8. ROS generation *in vitro*

ROS generated by GNR-DIsH and GNR-H was detected with the Fluorometric Intracellular ROS kit (Sigma-Aldrich), following the protocol provided by the manufacturer. Cells without nanoplatforms were used as a negative control, and 100% ROS was induced by adding $H_2O_2$ (800 μM, 33% w/v) as a positive control. For full details of the experimental setup and conditions, refer to section S6 of the SI.

### 2.9. Intracellular release of bioactive agents

The light-activated intracellular release of DOXO, PLL@ICG and siRNA-FITC from the GNR-DIsH nanoplatform was evaluated by fluorescence quantification in HeLa and Balb/3T3 cells. Cells were incubated with the nanoplatform for 6 h and washed with PBS to remove non-internalized nanostructures. After that, the samples were subjected to irradiation at 5, 7, and 11 h using an 808 nm diode laser (power densities: 1.0 and 2.0 W $cm^{-2}$; irradiation time: 5 min). Fluorescence intensity of the bioactive compounds was recorded hourly up to 12 h and at 24 h using a FLUOstar OMEGA plate reader. Full experimental details are provided in section S7 of the SI.

### 2.10. Cell uptake by fluorescence microscopy and TEM

The uptake of the nanoplatforms by HeLa and Balb/3T3 cells was monitored using fluorescence and transmission electron

microscopy (TEM). Full details of the experimental conditions and setups are provided in section S8 of the SI.

### 2.11. Inhibition of PD-L1

Quantitative real-time polymerase chain reaction (qRT-PCR) was used to determine the difference in PD-L1 expression before and after treatment with the GNRs-DIsH nanoplatforms. Briefly, total RNA was extracted from HeLa cells using the Trizol reagent (Invitrogen) according to the manufacturer's instructions. Quantitative PCR for PD-L1 was performed using Maxima SYBR Green qPCR Master Mix (Thermo Fisher). The expression of the target RNA relative to the reference gene GAPDH was calculated based on the threshold cycle (Ct) as $R = 2^{-\Delta(\Delta Ct)}$, where ΔCt is the difference between the Ct of the target gene and the Ct of GAPDH, while Δ(ΔCt) is the difference between ΔCt of siRNA-treated cells and ΔCt of untreated cells. The Ct (threshold cycle) values were determined using the real-time PCR system. The primer nucleotide sequences for PCR are presented in Table S1.

### 2.12. Cell death mechanism assay

Annexin V-propidium iodide (PI) flow cytometry assay was used to study the mechanism of cell death. For a comprehensive description of the experimental setup and conditions, refer to section S9 of the SI.

### 2.13. Statistical analysis

The results are reported as mean ± standard deviation ($n = 3$) and analyzed using a two-tailed *t*-test for comparisons between two groups, and one-way ANOVA with Tukey's *post-hoc* tests for multiple group comparisons. A 99% confidence interval ($p < 0.01$) was considered statistically significant.

## 3. Results and discussion

### 3.1. Synthesis and characterization of GNRs-based nanoplatforms

GNRs were synthesized by a wet-chemical method based on the controlled growth of CTAB-capped gold seeds through the sequential addition of $AgNO_3$ and ascorbic acid. The obtained nanostructures were highly monodisperse and exhibited a well-defined rod-like morphology, with dimensions of 31.0 ± 3.8 nm in length and 8.1 ± 1.0 nm in width (Fig. 1A and S1D and E). Although the synthesized GNRs were carefully washed by centrifugation, it is well known that traces of inherently cytotoxic CTAB can remain on the surface of GNRs, thus potentially compromising their biocompatibility.[31] In order to mitigate this cytotoxicity while providing the nanoplatforms with both colloidal stability and the intended multitherapeutic capability, a complex multilayered polymeric coating was deposited surrounding the GNRs. Thus, the plasmonic nanostructures were surface-modified through a layer-by-layer method with positively and negatively charged polymers, along with the bioactive compounds DOXO, ICG, and siRNA (Fig. 1B). The nanoplatforms were finally covered with HA to provide them with tumor-targeting capability.

To clarify the driving forces underlying the layer-by-layer self-assembly of our surface-engineered GNRs, we highlight that the process is primarily governed by electrostatic and hydrophobic interactions, with π–π stacking interactions also contributing at specific stages. The initial adsorption of PSS onto CTAB-stabilized GNRs is mainly electrostatic, facilitated by the opposite charges of PSS and residual CTAB molecules. Hydrophobic interactions between the aliphatic chains of CTAB and the aromatic groups of PSS may further stabilize this layer.[32] Subsequent adsorption of DOXO onto the PSS layer involves both electrostatic attraction and hydrophobic interactions, and π–π stacking between the anthracycline moiety of DOXO and the aromatic groups of PSS may also play a role.[33] The subsequent layers, including PLL@ICG, siRNA, and hyaluronic acid (HA), are assembled through a combination of electrostatic attraction and weaker non-covalent interactions such as π–π stacking, for instance between ICG and DOXO.[34] Together, these interactions ensure the stable and sequential construction of the multilayered nanoplatform.

The adsorption of the successive polymeric layers and bioactive agents onto GNRs was monitored through UV-vis spectrophotometry and ζ-potential measurements. These revealed progressive shifts in the longitudinal and transversal localized surface plasmon resonance (LSPR) bands, reflecting the successful deposition of the polymers and bioactive compounds (Fig. 1C and D). In particular, the longitudinal LSPR peak, initially located at ~792 nm, exhibited a red shift to ~800 nm. These changes in the intensity and position of the LSPR peaks were attributed to the extreme sensitivity of GNRs to the dielectric properties of their surrounding environment.[35,36]

The sequential adsorption of polymers and bioactive compounds was also tracked by the changes in ζ-potential (Fig. 1E). A complete inversion of the surface charge of the GNRs from an initial value of 37.8 ± 0.6 mV to −56.4 ± 0.9 mV occurred after coating the nanostructures with a PSS layer. Afterwards, the surface charge of the nanoplatform increased to −22.0 ± 1.6 mV upon the addition of DOXO, an effect associated with the amino groups of the drug.[37] Then, a complete charge inversion to 31.3 ± 6.0 mV was observed after incorporating the positively charged PLL@ICG conjugate in the formulation of the nanoplatform. Subsequently, the deposition of the siRNA and HA layers modified the ζ-potential values to −17.7 ± 0.4 mV and −9.3 ± 0.6 mV, respectively. Thus, the performed multistep functionalization procedure resulted in a nanoplatform with a slightly negative surface charge that ensured its electrostatic stability while allowing its interaction with cells and receptor-mediated endocytosis.[38]

The changes in the characteristics of the nanoplatform upon the attachment of the successive coating layers were further analyzed by TEM and dynamic light scattering (DLS). Microscopy images revealed no significant degradation, morphological alterations, and/or substantial particle aggregation throughout the different coating steps (Fig. 1F). On the other hand, DLS measurements confirmed the successful adsorption

 

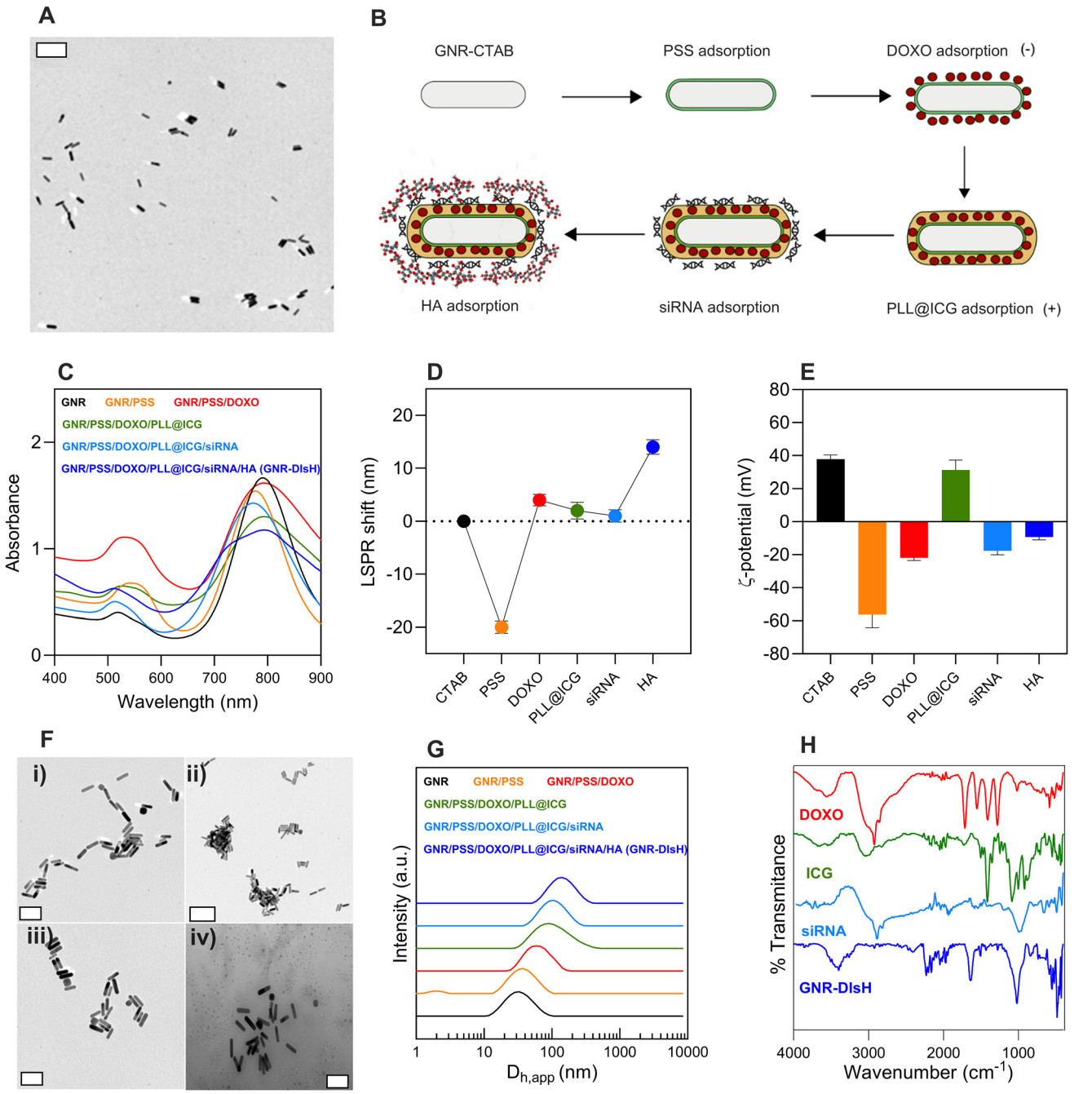


**Fig. 1** (A) TEM image of the as-synthesized GNRs (scale bar = 100 nm). (B) Schematic illustration of the layer-by-layer process used to produce GNR-DIsH. (C) UV-vis spectra of the GNRs-based nanoplatform after the successive addition of polyelectrolytes and bioactive molecules (PSS → DOXO → PLL@ICG → siRNA → HA). (D) Shift of the longitudinal LSPR peaks and (E) ζ-potential values after the deposition of the successive coating layers. (F) TEM images of the GNRs-based nanoplatform at different stages of its functionalization process: after the addition of (i) PSS-DOXO, (ii) PLL@ICG, (iii) siRNA, and (iv) HA (i, iii, iv: scale bar = 50 nm; ii: scale bar = 100 nm). (G) Hydrodynamic diameter of the nanoplatform after the deposition of each coating layer. (H) FTIR spectra of free DOXO, free ICG, siRNA and GNR-DIsH.

of polymeric and drug layers surrounding the GNRs, when a progressive increase in the hydrodynamic size of the nanoplatform from 32.7 ± 4.2 nm for bare GNRs to 142 ± 14 nm after the deposition of the final HA layer was observed (Fig. 1G). The relatively narrow size distributions obtained by DLS indicated the absence of large aggregates, with only small clusters possibly forming during the multicoating process. The successful formation of the different layers surrounding the synthesized GNRs was finally corroborated by FTIR, with the spectra of free DOXO, ICG and siRNA recorded as controls and used to identify different vibrational modes (Fig. 1H). The FTIR spectrum of the complete nanoplatform revealed the

characteristic vibrational modes of DOXO at 1550, 1712, 2867, and 2929 $cm^{-1}$, ICG at 1398, 1631, 1481, and 2813 $cm^{-1}$, and siRNA-FITC at 3434, 2086, and 1637 $cm^{-1}$, thus confirming the successful encapsulation of the bioactive compounds within the designed nanoplatform.[39,40] The details of the bonds/vibrational modes associated with each band can be found in section S10 of the SI.

### 3.2. Entrapment efficiency and drug loading capacity

Following the optical and physicochemical characterization of the nanoplatform, the entrapment efficiency and drug loading capacity were evaluated for each bioactive compound. To this end, the amounts of DOXO, PLL@ICG, and siRNA that remained in the supernatants after each functionalization step were quantified.

In this way, it was established that up to 350 μg (0.644 μmol) of DOXO were encapsulated within the designed nanoplatform, corresponding to an EE% of 92.0%. This value surpasses those reported in previous studies employing polymer-coated,[41] mesoporous silica-coated,[42,43] and PSS-coated GNRs,[44] confirming the high encapsulation efficiency achieved by our layer-by-layer functionalization and loading strategy. Considering the total mass of the nanoplatform after DOXO loading, it was established that this encapsulation value corresponds to a DL% of 62.1% for this drug. Interestingly, this value lies at the upper range for gold-based DOXO nanocarriers, particularly those coated with polymeric layers, which typically report DL% values between 10% and 55%.[45–47] While higher loadings can be achieved with extremely porous shells, such as mesoporous silica or metal organic frameworks, these materials suffer from significant drawbacks, including limited structural stability in biological media, premature drug leakage, or potential concerns regarding long-term biodegradability and biocompatibility.

On the other hand, the EE% and DL% for ICG in the designed nanoplatform were determined as 84.0% and 42.7%, respectively. These values compare favorably with existing gold-based nanosystems, many of which display lower or unreported ICG loading when using polymer or even silica shells, underscoring the high ICG loading capacity of our design.[48–51] Finally, the EE% of siRNA was also calculated, yielding a value of 89.2%, which is in close agreement with the values reported in previous studies.[52–54] The DL% of siRNA was not reported, since this metric is rarely used for nucleic acids: owing to their very low mass relative to the nanoplatform, the calculated values are negligible and provide little biological relevance, whereas EE% is the standard and more informative parameter. Collectively, these results confirm the excellent encapsulation capability of our nanoplatform for the different bioactive compounds.

### 3.3. Colloidal stability

The colloidal stability of GNR-DIsH was evaluated in aqueous environments and different complex biological media. As shown in Fig. 2A, the nanoplatforms were completely stable under both basic and physiological conditions (pH 9.0 and 7.4, respectively), showing negligible variations in their hydrodynamic size over a six-day incubation period. However, when exposed to pH 5.0, the hydrodynamic diameter of the nanoplatforms progressively increased from 100 ± 25 nm to 324 ± 22 nm after 96 h of incubation, accompanied by a remarkable shift in their surface charge from −10.0 ± 1.3 mV to −7.6 ± 0.9 mV, respectively (Fig. 2B). Likewise, upon exposure to pH 3.5, the size of the nanoplatforms increased from 326 ± 56 nm to 602 ± 36 nm, following a trend similar to that observed at pH 5.0 (Fig. 2B). The significant increase in hydrodynamic diameter upon incubation in acidic media (pH 3.5 and 5.0) was likely due to nanoparticle aggregation. This aggregation may result from the protonation of negatively charged carboxyl groups in the PSS and HA layers, leading to a reduction in electrostatic repulsion between particles.[37]

In terms of surface charge, a consistent trend toward less negative ζ-potential values was observed at pH 3.5, 5.0, and even 7.4. This behavior may result from the local accumulation of positive counterions near the nanoparticle surface and/or the partial release of outer HA chains, exposing the underlying positively charged PLL layer. On the other hand, the ζ-potential of the multilayer-coated GNRs decreased under basic conditions (pH 9.0), which may indicate the gradual release of the outer polymer layers and the bioactive compounds over time, ultimately exposing the PSS layer.

In addition to the influence of pH, the presence of serum proteins in the incubation media supplemented with 10% FBS, also led to remarkable increases in the size of the nanoplatforms, with these increases being attributed to the formation of the protein corona from the early stages of the incubation process (Fig. 2C). The adsorption of serum proteins was also the cause of significant decreases in the magnitude of ζ-potential (Fig. 2D). In contrast, when a protease such as trypsin was also incorporated into the incubation medium, the size of the nanoplatforms remained intact during the first 96 h. This suggests that trypsin was able to degrade the corona formed by the proteins present in FBS, leading to smaller sizes in the presence of the protease compared to the enzyme-free control. However, after 96 h, a sudden increase in particle size occurs, which can be associated with the formation of aggregates as in previous cases. Notably, upon exposure to trypsin, the ζ-potential of the nanoplatform increased from −13.3 ± 2.9 to −10.1 ± 2.5 mV during the first 72 h of incubation, followed by a sharp rise to −3.2 ± 0.5 mV, suggesting a gradual degradation of the PLL layer (Fig. 2D).

### 3.4. Release kinetics of bioactive agents

After assessing the colloidal stability of the nanoplatform under different environmental conditions, we next evaluated the release profiles of DOXO, PLL@ICG and siRNA from GNR-DIsH in PBS at pH 7.4 and 5.0 and supplemented with 10% (v/v) FBS, both in the presence or absence of a proteolytic enzyme (3.125 mg $L^{-1}$) and NIR light stimulus.

In the absence of stimuli, the release profiles exhibited an initial lag phase within the first 2–3 h of incubation for DOXO and PLL@ICG, while this phase extended up to 6–8 h for

 

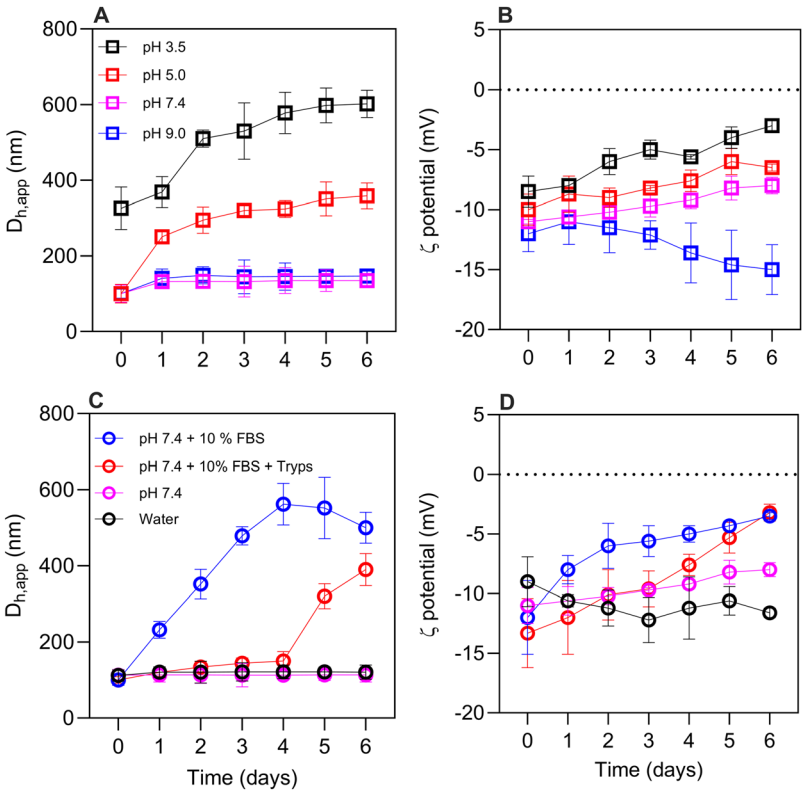


**Fig. 2** Evaluation of the colloidal stability of the GNR-DIsH nanoplatform at 37 °C by monitoring the time evolution of its (A) hydrodynamic diameter and (B) ζ-potential at different pH values; and its (C) hydrodynamic diameter and (D) ζ-potential in water and PBS supplemented with 10% FBS and 10% FBS + trypsin.

siRNA. Following this, a burst release phase after 12 h of incubation was observed in all cases and under all conditions, after which a slower and sustained release phase was noted (Fig. 3A and B).

Additionally, it was observed that the proportion of released DOXO was slightly higher under acidic conditions than that at physiological pH. This was attributed to the increased electrostatic repulsion between the protonated DOXO molecules and the positively charged PLL chains in acidic environments.[55] Under these conditions, it was observed that DOXO, despite being located within a more internal layer of the platform coating, was released most rapidly, followed by siRNA and the PLL@ICG conjugate. The faster release of DOXO may be related to the molecular size difference compared to siRNA and PLL@ICG, which could influence its diffusion through the polymeric coating.[56] In contrast, the release of the PLL@ICG conjugate remained relatively minimal and slow (about 20%), indicating that the platform interactions between negatively charged PSS and positively charged PLL were strong and largely insensitive to the acidic medium.

When trypsin, an enzyme capable of breaking peptide bonds, such as those found in PLL, was incorporated into the incubation medium, a significant increase in the proportions of released bioactive compounds was observed, attributed to the enzymatic degradation of the PLL@ICG layer, which facilitated the diffusion of the cargo from the platform (Fig. 3C and D). A similar effect occurred upon the application of an external stimulus such as NIR light. The nanoplatform was irradiated at power densities of 1.0 and 2.0 W $cm^{-2}$ for 5 min at different time points between 2 and 48 h of incubation, leading to a marked increase in the amounts of released bioactive agents (Fig. 3E–L) when compared to those established in the absence of light exposure.

The nanoplatforms exhibited high sensitivity to NIR light due to the plasmonic properties of GNRs and the presence of the NIR-absorbing dye ICG. Thus, higher concentrations of released bioactive molecules were observed upon the application of increased laser power densities. Interestingly, the application of NIR light at specific intervals during the release process resulted in rapid release immediately after the light stimulus, followed by a gradual slowdown and stabilization over time (see the arrows in Fig. 3E).

Furthermore, the use of NIR light allowed for more effective control over drug release, reducing the initial delay phase (up to 3–4 h incubation) and enhancing the release kinetics, thus potentially preventing the delivery of sub-therapeutic concentrations that could fail in achieving the desired pharmacological effect and/or cause adverse physiological outcomes. Unfortunately, the excellent initial control of the release profile was not fully maintained at longer incubation times

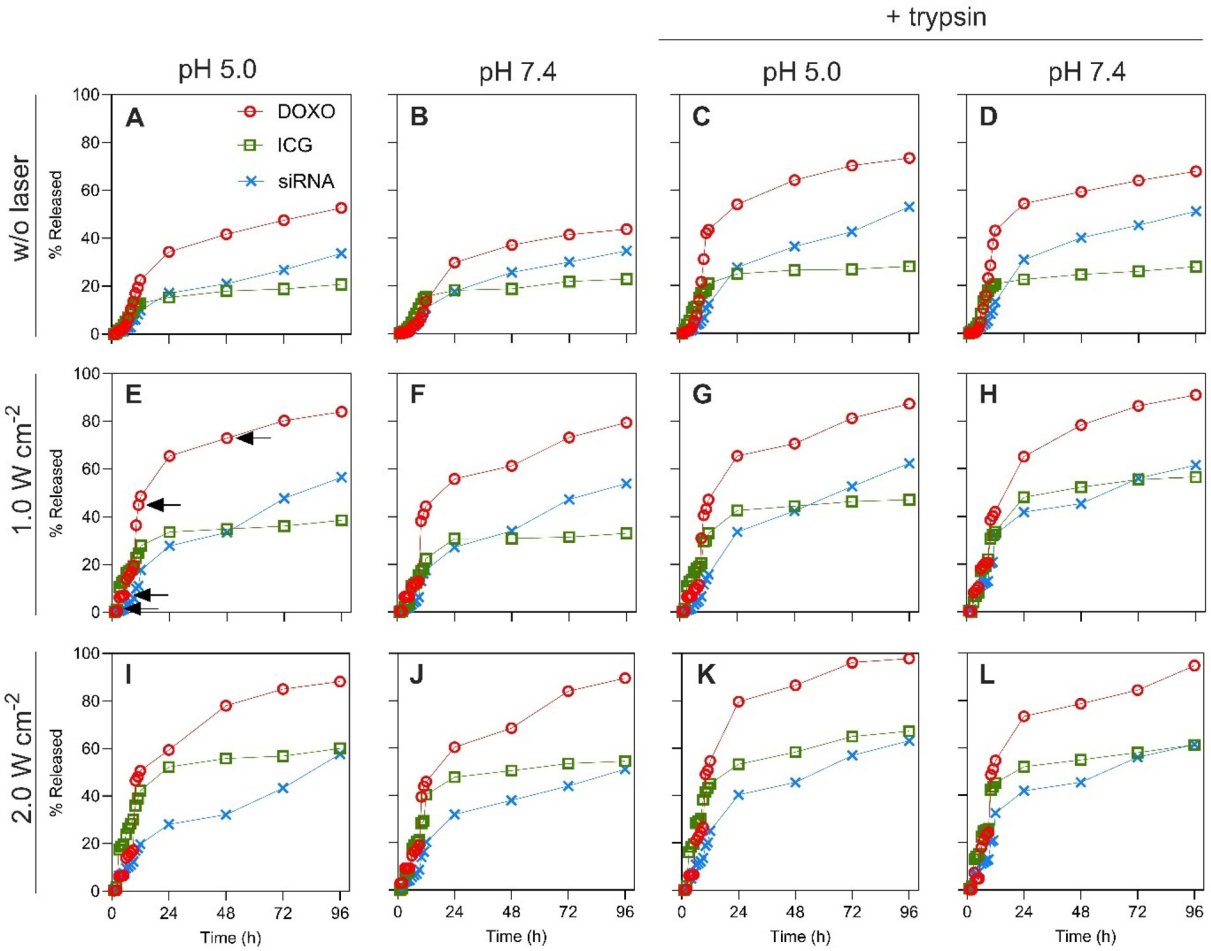


**Fig. 3** Release profiles of the different bioactive compounds from the GNR-DIsH nanoplatform, (A–D) without laser irradiation, and under exposure to (E–H) 1.0 and (I–L) 2.0 W $cm^{-2}$ NIR irradiation. In each case, release profiles were determined at pH 5.0 and 7.4, in both the absence and presence of trypsin, as indicated at the top of the figure ($n$ = 3; error bars are not shown for clarity).

due to the progressive destabilization of the nanoplatform coating caused by successive light irradiations (see the arrow at 48 h in Fig. 3E).

Overall, the cargo amounts released in the presence of NIR irradiation were slightly higher than those observed in the presence of the enzyme without light stimulation. This fact suggests that localized heating on the nanoplatform surfaces due to NIR irradiation could alter the interactions between the polyelectrolytes and the bioactive agents more than enzymatic degradation, thus further destabilizing the coating and promoting the diffusion of DOXO, siRNA and the PLL@ICG conjugate.

Finally, when both enzymatic degradation and NIR irradiation were simultaneously applied to modulate the release process, it was observed that a nearly complete release of encapsulated DOXO and a large release of siRNA were achieved (Fig. 3G, H and 3K, L). The total amount of bioactive molecules released from the nanoplatform into the surrounding medium was highest among all the tested conditions, with a slightly higher release degree observed at acidic pH. In this combined approach, light action complemented the hydrolysis of PLL peptide bonds by trypsin, progressively degrading the PLL layer. Additionally, the simultaneous application of protease and laser light resulted in faster release kinetics compared to either stimulus alone, resulting in the staircase-like release profile associated with maintained light stimulation. The percentages of DOXO, siRNA, and PLL@ICG released after 96 h incubation under all of the different applied conditions are summarized in Table S3 in the SI.

### 3.5. Cytocompatibility and cellular uptake of the nanoplatform

The potential inherent cytotoxicity of the nanoplatform was first evaluated by incubating GNR-DIsH with Balb/3T3 mouse fibroblasts and HeLa cancer cells for 24 and 48 h in the absence of any type of endogenous (enzyme degradation) or exogenous (NIR light) stimulus. The HeLa cell line was selected due to its overexpression of CD44,[25,27] which is one of the two main specific receptors of HA.[57] Furthermore, the HeLa cell line highly expresses PD-L1.[24,26] This makes HeLa cells a relevant model for studying the influence of active targeting on the therapeutic and gene-silencing activity of GNRs

as a non-viral transfection vehicle for PD-L1 siRNA. In contrast, Balb/3T3 fibroblasts express low levels of CD44 on their cell membrane,[28] and are not responsive to human PD-L1 siRNA, making them an adequate control cell line. Moreover, the Balb/3T3 cell line is commonly used to analyze the potential toxic effects of bioactive compounds and nanomaterials because of its extraordinary sensitivity to external agents.[58] Positive control groups included free DOXO, free ICG, and Lipofectamine 2000 + siRNA, while the negative control consisted of the nanoplatform functionalized with HA but without encapsulated bioactive agents (GNR-H).

As shown in Fig. 4A, the GNR-H nanoplatform without encapsulated bioactive agents exhibited negligible toxicity in both cell lines when incubated at $2.5 \times 10^{10}$ NPs per mL concentration, with cell viabilities close to 100%. On the other hand, a slight reduction in the viability of HeLa cells to 95%

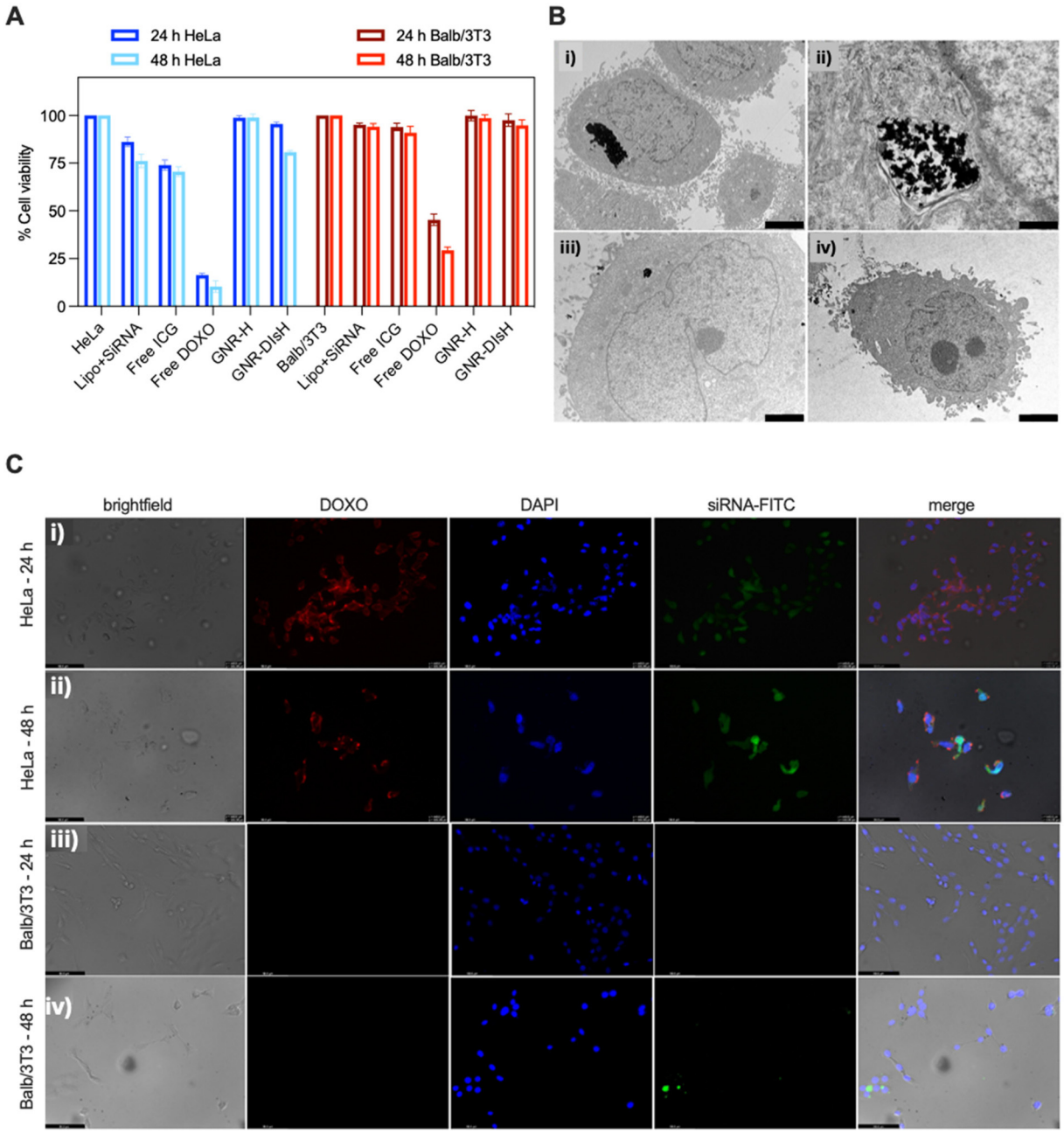


**Fig. 4** (A) Cell viability of HeLa and Balb/3T3 cells after 24 and 48 h of incubation with Lipofectamine + siRNA complex, free ICG (20 μM), free DOXO (12.5 μM), GNR-H (control) and GNR-DIsH at 37 °C and $2.5 \times 10^{10}$ NPs per mL concentration. (B) TEM images of the cellular uptake of GNR-DIsH in (i: scale bar = 4 μm; ii: scale bar = 400 nm) HeLa and (iii: scale bar = 1 μm; iv: scale bar = 4 μm) Balb/3T3 cells after 24 h of incubation. (C) Cell uptake of the GNR-DIsH nanoplatform in HeLa and Balb/3T3 cells after 24 and 48 h of incubation. Blue coloration corresponds to the cell nuclei stained with DAPI ($\lambda_{ex/em}$ = 357/447 nm), red denotes the fluorescence of DOXO ($\lambda_{ex}/_{em}$ = 585/624 nm), and green corresponds to the fluorescence of siRNA-FITC ($\lambda_{ex/em}$ = 488/520 nm).

and 81% were observed after 24 and 48 h incubation with GNR-DIsH, and 98% and 94% in the case of Balb/3T3 cells. These results provide initial evidence of the role of CD44 receptor overexpression on the HeLa cell membrane, which will be discussed in more detail below.

In contrast, significantly higher toxicity was observed in the case of free DOXO when incubated at an equivalent concentration to that when encapsulated in the platform (12.5 μM), with viabilities of HeLa cells dropping to 17% and 10% after 24 and 48 h incubation, respectively, with corresponding values of 45% and 29% in the case of Balb/3T3 cells.

The administration of free ICG (20 μM) resulted in lower cytotoxicity degrees, with viabilities of 74% and 70% for HeLa cells, and 94% and 91% for Balb/3T3 cells upon 24 and 48 h of incubation. The observed cytotoxicity of the Lipofectamine + siRNA complex (425 pmol siRNA) can be primarily attributed to cationic lipid used to form the polyplex,[59] although PD-L1 silencing by siRNA may also contribute to reduced cancer cell proliferation.[60]

Next, the cellular uptake of the nanoplatform was evaluated using TEM and fluorescence microscopy. In this way, TEM images confirmed the successful internalization of GNR-DIsH into HeLa cells after 24 h of incubation, being that the nanoplatforms are primarily localized within endosomal vesicles within the cytoplasm Fig. 4(Bi and ii). In contrast, a much lower internalization of the nanostructures was observed in the case of Balb/3T3 cells (Fig. 4Biii and iv).

To further corroborate the capability of the nanoplatforms to transfect siRNA, HeLa cells were incubated with GNR-DIsH for 24 and 48 h. GNR-DIsH internalization was monitored by exploiting the fluorescence of DOXO (emission peak at 600 nm), and FITC-labeled scrambled siRNA (emission peak at 519 nm). As shown in Fig. 4Ci, the nanoplatform was efficiently internalized by HeLa cells after 24 h of incubation, probably through a receptor-mediated endocytosis mechanism. Interestingly, the loaded DOXO was initially localized in the cytoplasm, before being progressively incorporated into the cell nuclei. Moreover, siRNA-FITC was already detected in the cellular cytoplasm after 24 h incubation, with its presence increasing at 48 h, thus indicating a sustained release of the genetic material (Fig. 4Cii). The high internalization degree of the designed nanoplatform in HeLa cells can be attributed to the high affinity of HA for the CD44 receptors overexpressed on the membrane of these cells,[27] along with their elevated metabolic activity.[61] Finally, it is worth noting that after 48 h incubation, HeLa cells displayed altered morphologies that were more rounded, likely due to the cytotoxic effect of DOXO.

On the other hand, the uptake of the nanoplatform by Balb/3T3 cells was significantly lower, as previously inferred from TEM images and from the reduced fluorescence of DOXO and siRNA observed in the cytoplasm (Fig. 4Ciii and iv). This observation correlates with the lack of toxicity of the nanoplatform in this cell line as determined above, which is due to the low internalization degree attributed to the absence of CD44 receptors on the surface of Balb/3T3 cells. Furthermore, electrostatic repulsive interactions between the negatively charged nanosystem and cell membranes may have also contributed to hinder higher cellular uptake.[62]

### 3.6. Light-activated ROS generation

After confirming that the designed multilayered nanoplatforms exhibited negligible cytotoxicity in the absence of external stimuli, we evaluated the intracellular production of ROS in HeLa cells upon light stimulation. *In vitro* ROS production was assessed by irradiating the nanostructures for 5 or 10 min at power densities of 1.0 or 2.0 W $cm^{-2}$. The effect of the medium temperature (4, 25, or 37 °C) was also analyzed to distinguish the contributions of both photodynamic and photothermal effects on cellular cytotoxicity (as detailed below). Untreated cells and cells incubated in the presence of $H_2O_2$ (800 μM), or GNR-H were used as controls.

The impact of the irradiation power density and time was first evaluated, which established that an increased laser power density (from 1.0 to 2.0 W $cm^{-2}$) resulted in a higher production of ROS. For instance, after 5 min of irradiation at 37 °C, 1.0 W $cm^{-2}$ and 6 h of incubation, the ROS level was 53%. When the laser power density was increased to 2.0 W $cm^{-2}$, ROS production rose to 74% under the same conditions (Fig. 5A and E). Furthermore, ROS generation was also enhanced by extending the irradiation time from 5 to 10 min at 2.0 W $cm^{-2}$, reaching 83% (Fig. 5E and M).

Regarding the effect of drug–light interval, defined as the time lapse between the administration of the photosensitizer and the exposure to the light source,[63] we observed a reduction in ROS production with increasing intervals. For example, at a power density of 1.0 W $cm^{-2}$ applied at 37 °C for 5 min after 6 h of incubation, ROS generation was 53%. However, when cells were co-cultured with nanoplatforms for 48 h, the ROS production decreased to 45% (Fig. 5A and D). This behavior may result from the combination of cell death induced by DOXO and a loss of the photostability of the photosensitizer after prolonged exposure to cell culture conditions (37 °C and high protein concentrations). Moreover, changes in the colloidal stability of the nanoplatforms inside the cells could contribute to the diminished ROS generation over time. Thus, for example, in the incubation interval from 6 to 12 h, ROS production remained between 70 and 80% relative to the positive control under 2.0 W $cm^{-2}$ irradiation (Fig. 5E, F and 5M, N), while within the interval from 24 to 48 h it decreased to *ca.* 45–65% (Fig. 5G, H and 5O, P).

The local temperature of the medium did not appear to be a parameter that significantly affects the ROS generation capability of the nanoplatform in the performed experiments. Nevertheless, in certain cases, there was a weak correlation between higher local temperatures and increased ROS production (Fig. 5H).

In summary, the thorough evaluation of ROS production under various light dosages, incubation times, and environmental temperatures emphasized the key role of the drug–light interval and light dosage in ROS generation. The obtained results constitute a valuable insight for the design of future *in vivo* preclinical studies.[64,65]

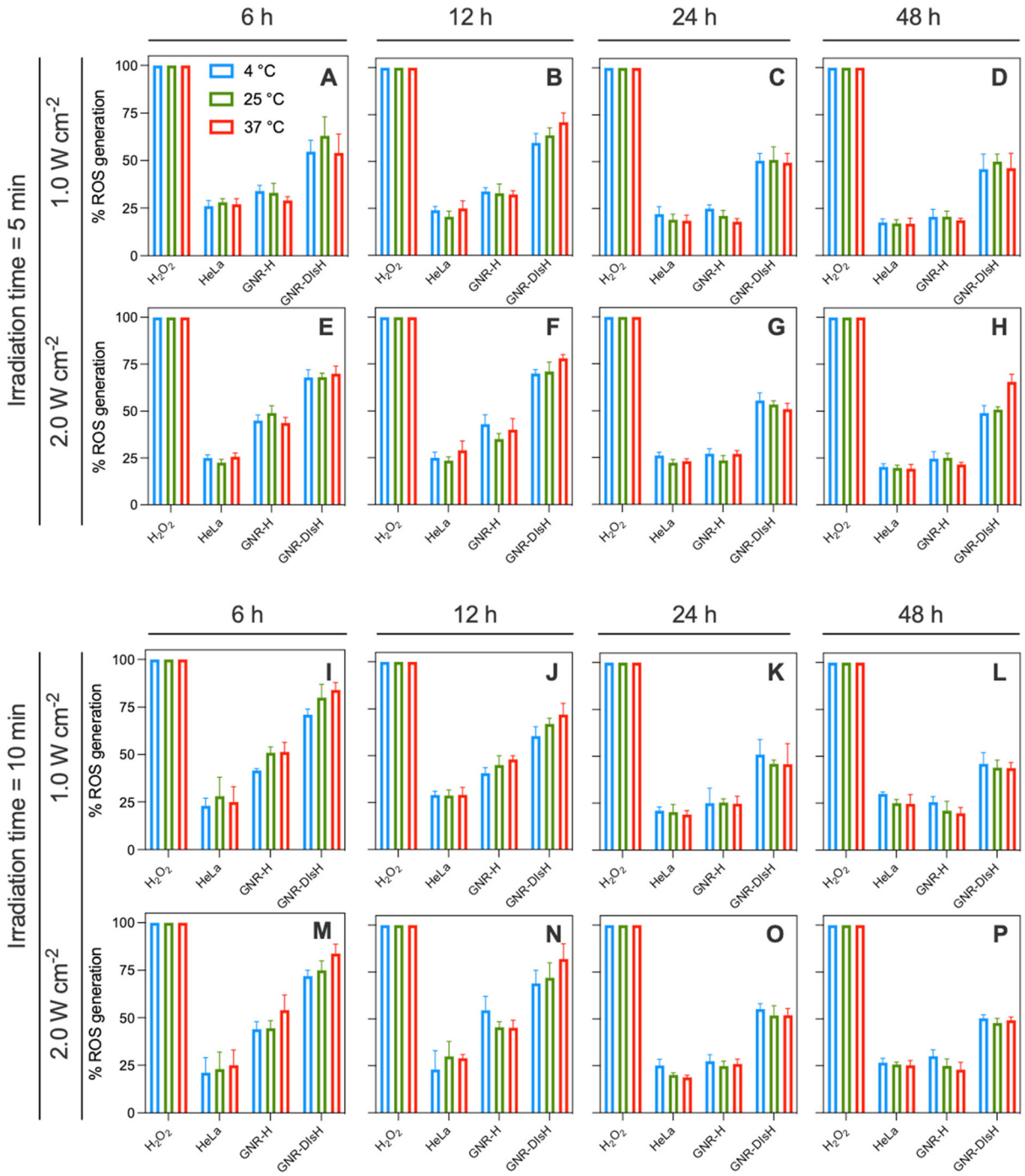


**Fig. 5** ROS generation by GNR-DIsH NPs after their incubation for 6, 12, 24, and 48 h in HeLa cells. The local temperature of the medium was 4, 24 or 37 °C and the samples were irradiated for 5 min (A–H) and 10 min (I–P) using laser power densities of 1.0 and 2.0 W $cm^{-2}$. $H_2O_2$ (800 μM) was used as a positive control, and untreated HeLa cells as a negative control. The GNR-H nanoplatform was used as an additional control.

### 3.7. Light-activated cytotoxicity

The next step in the evaluation of the nanoplatform was assessing the multimodal *in vitro* therapeutic activity. For that, the CCK-8 assay was used to measure cell viability of HeLa and Balb/3T3 cells treated with the individual bioactive agents and GNR-H, or GNR-DIsH for 24 or 48 h, and irradiated at 4, 25 or 37 °C with laser power at 1.0 or 2.0 W $cm^{-2}$. As depicted in Fig. 6A, the application of NIR irradiation (1.0 W $cm^{-2}$, 5 min) after 24 h incubation resulted in significantly lower viabilities of HeLa cells when they were incubated with the GNR-DIsH nanoplatform, compared to individual treatments with free DOXO, free ICG, Lipofectamine + siRNA polyplex, or GNR-H. This inhibitory effect increased with prolonged incubation

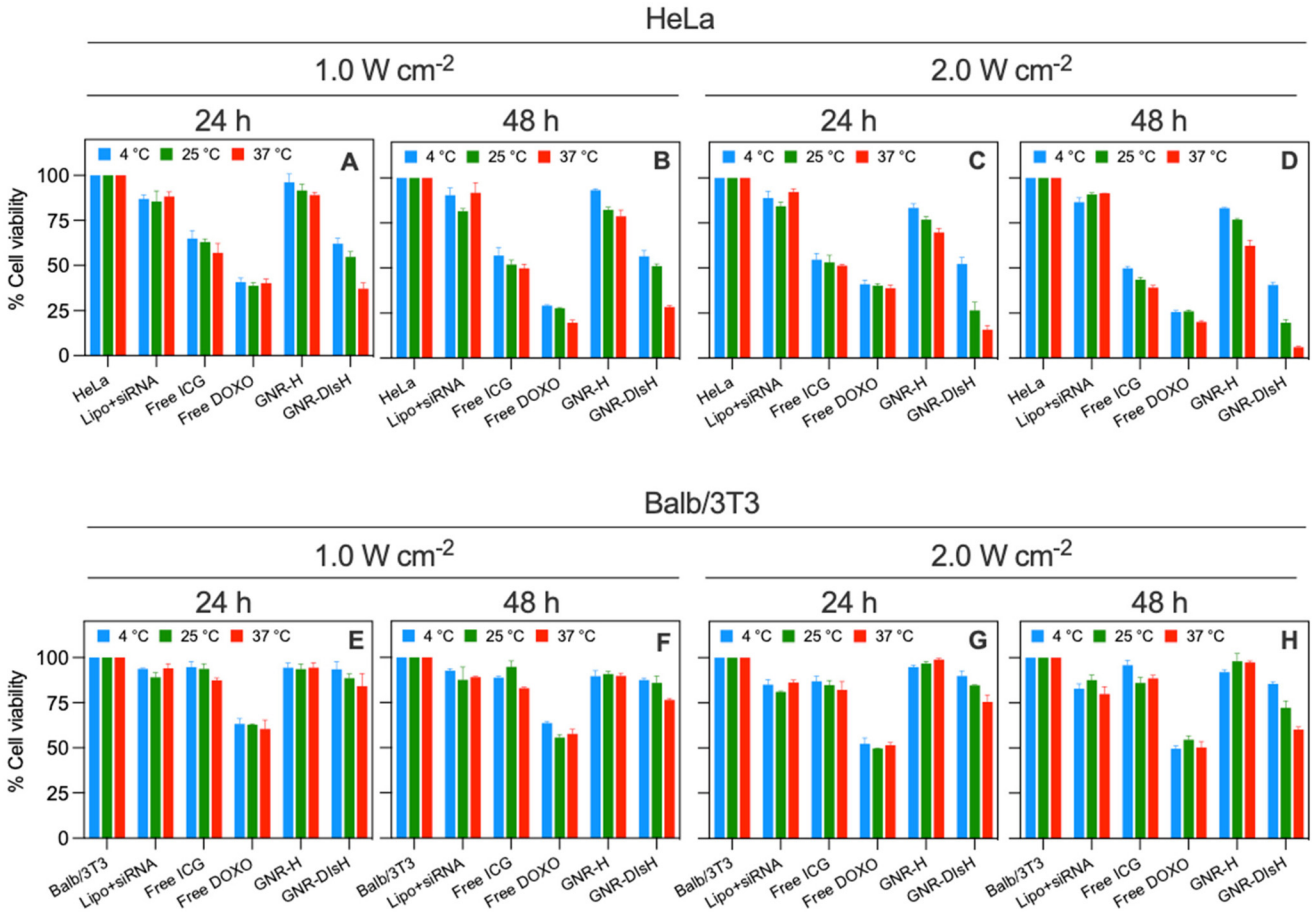


**Fig. 6** Cell viability of (A–D) HeLa and (E–H) Balb/3T3 cells after NIR irradiation at 4, 25 and 37 °C, and at 1.0 and 2.0 W $cm^{-2}$ for 5 min after 24 or 48 h of incubation with free DOXO, free ICG, Lipofectamine + siRNA complex, GNR-H and GNR-DIsH.

times (Fig. 6B), particularly at 37 °C. The observed cytotoxic effect of the GNR-DIsH was attributed to the combined activities of ROS generated by the encapsulated ICG, the chemical action of DOXO, and the hyperthermic effect of ICG-driven PTT, and plasmonic PTT.

The sustained release of the bioactive agents from the nanoplatform led to their intracellular accumulation, reaching an effective therapeutic concentration that significantly reduced cell viability compared to the administration of free compounds. On the other hand, when the NIR irradiation power density was increased to 2.0 W $cm^{-2}$, GNR-DIsH showed an even larger cytotoxic effect, surpassing the inhibitory activity of free DOXO. This enhanced synergistic effect can be explained by the increased release of DOXO, siRNA, and PLL@ICG inside the cells triggered by higher laser fluencies.

As expected, the combined effect of PTT, PDT, gene silencing, and chemotherapy resulted in an almost complete inhibition of cancer cell viability under the evaluated conditions. It is also worth mentioning that the therapeutic role of PDT can be confirmed by observing the higher cell toxicity achieved at 4 °C after 24 and 48 h of incubation, compared to the values obtained after the administration of the nanoplatform lacking DOXO, siRNA and PLL@ICG (GNR-H). At low temperatures, the photothermal effect was insufficient to induce significant cytotoxicity *via* PTT or a sufficient release of DOXO for effective chemotherapy. Therefore, the observed toxicity originated from ROS produced by the photosensitizer.

In contrast, neither the Lipoplex with siRNA nor free ICG induced significant cell death when administered to Balb/3T3 murine fibroblasts under the tested conditions, reaching a maximum inhibition of 20% for both bioactive agents (Fig. 6E–H). However, administration of free DOXO induced notable reductions in cell viability, ranging from 50–60%, depending on the temperature and incubation time, although these effects were less pronounced than in cancer cells. This difference was attributed to the accelerated metabolism of HeLa cells, which make them more susceptible to the action of the antineoplastic drug.[66] For the GNR-H platform (without bioactive compounds), the cytotoxic effect on Balb/3T3 cells was almost negligible because of the reduced internalization of the nanosystem, as previously confirmed by fluorescence microscopy and TEM, and the absence of active targeting mechanisms in this cell line. However, the complete GNR-DIsH nanoplatform exhibited slightly higher cytotoxicity on Balb/3T3 cells. Viability values of 89, 85, and 76% at 4, 25, and 37 °C after 24 h incubation and 86, 74, and 63% after 48 h

incubation, were established when cells were irradiated for 5 min at 2.0 W $cm^{-2}$ (Fig. 6G and H). This reduced viability resulted from the chemotherapeutic action of DOXO, which can passively diffuse into the cytoplasm when released in the vicinity of cell membrane, as well as from the generation of ROS in the extracellular environment, since the concentration of bioactive agents inside the cells remained low.

In summary, the results obtained in this section suggest that the therapeutic efficacy of the designed GNR-DIsH nanoplatform is maximized under 2.0 W $cm^{-2}$ NIR irradiation at physiological temperature, yielding a potent synergistic cytotoxic effect, particularly against HeLa cancer cells.

### 3.8. Intracellular laser-activated release of bioactive compounds

To shed light on the remote responsiveness of the designed nanoplatform, we evaluated the intracellular release kinetics of the encapsulated bioactive agents following NIR light irradiation at different timepoints and laser power densities. Fig. 7A–D indicates the amounts of PLL@ICG, DOXO, and siRNA released over time inside HeLa and Balb/3T3 cells during a 24 h incubation period, with samples irradiated at 1.0 or 2.0 W $cm^{-2}$ at selected timepoints. Specifically, NIR irradiation was applied for 5 min at 5, 7, and 11 h post-administration of the nanoplatform (indicated by the dashed lines in Fig. 7A–D). In most cases, remarkable increases in the release of the bioactive compounds were observed after the application of the stimulus. Notably, HeLa cells exhibited a significantly higher release of bioactive compounds, even in the absence of light stimulation (Fig. 7A and C), consistent with earlier findings from epifluorescence microscopy images shown in Fig. 4C. In contrast, and as expected, the release of the bioactive cargoes was markedly lower when the nanoplatform was incubated with Balb/3T3 cells (Fig. 7B and D).

### 3.9. PD-L1 silencing

To further assess the efficacy of the designed GNR-DIsH in the delivery of the encapsulated bioactive compounds and to verify that PD-L1 siRNA retains its gene silencing activity when incorporated into the nanoplatform and released into the cell cytoplasm, we conducted a qRT-PCR analysis. As shown in Fig. 7E and F, in the absence of laser irradiation, the inhibition of mRNA expression levels is relatively low, which is consistent with the release data. However, upon exposure to NIR light, the silencing effect is significantly enhanced, with greater inhibition observed at higher laser power densities and longer incubation times (GNR-DIsH *vs.* GNR-DIsH + 2 W $cm^{-2}$, 72 h, $p < 0.001$). In contrast, free siRNA administration failed to induce gene silencing, probably due to the rapid degradation of genetic material by nucleases, while the transfection of siRNA with Lipofectamine led to PD-L1 expression levels similar to those obtained in the absence of NIR illumination. This highlights the superior gene silencing capability of the nanoplatform when coupled with NIR-triggered release. It is important to note that released siRNA retained its silencing activity despite the temperature reached after 5 min of laser irradiation at 1.0 W $cm^{-2}$ (43 °C) and at 2.0 W $cm^{-2}$ (47 °C) (Fig. 7F), consistent with the previously reported thermal stability of therapeutic siRNAs.[67]

### 3.10. Cell death mechanism

Finally, the cell death mechanism induced by the multimodal therapeutic action of the nanoplatform, which combines chemotherapy, PTT, PDT, and gene silencing, was decoupled and analyzed through flow cytometry. Studies were performed after 48 h of incubation of HeLa and Balb/3T3 cells with GNR-DIsH and NIR irradiation at 1.0 and 2.0 W $cm^{-2}$ for 5 min at 4, 25, and 37 °C. Control groups included untreated cells (HeLa and Balb/3T3), free DOXO and PLL@ICG, the Lipofectamine–siRNA lipoplex, and the GNR-H platform.

The administration of free DOXO (12.5 μM) led to cell death by apoptosis, with values in the range of 70–75% and 55–60% for HeLa and Balb/3T3 cells, respectively, after 48 h incubation depending on the temperature and irradiation conditions (Fig. S2A and S2B). Both cell lines predominantly exhibited early-stage apoptosis. Cellular apoptosis slightly increased with the applied laser stimulus and the associated temperature increase, which is consistent with the known synergistic cytotoxic effect of combining DOXO and hyperthermia.[68] Moreover, HeLa cells displayed significantly lower survival rates because of their highly accelerated metabolism, as previously mentioned. Balb/3T3 cells showed higher survival rates at 4 °C, likely due to the slower diffusion of the drug into the cells, which is an energy-dependent process.[69]

For free PLL@ICG treatment, the percentage of apoptotic cells ranged from 50 and 60% in HeLa cells, while these percentages decreased to 20–35% in Balb/3T3 cells (Fig. S2C and S2D). In this case, late apoptosis, characterized by the disintegration of cell membrane, was more prominent than early apoptosis, in which cells retain membrane integrity.[70] This difference was probably due to the distinct mechanisms of action of light-activated PTT/PDT, which involves photothermal damage and oxidative stress,[71] compared to the chemotherapeutic action of the anticancer drug, which triggers oxidative stress and topoisomerase II inhibition.[72] Likewise, in line with the cellular toxicity data, naked siRNA did not induce apoptosis or cellular necrosis by itself (Fig. S2E and S2F).

For the GNR-H platform, it was observed that HeLa cells exhibited necrosis at incubation temperatures of 25 and 37 °C, while early apoptosis predominated at 4 °C (Fig. S2G). Cellular survival was relatively high in these cases, since PTT alone was not sufficiently effective to eradicate cancer cells. At 25 and 37 °C, the rupture of cell membranes due to photothermal effects was probably the cause of necrotic cell death. Irradiation plays a key role in increasing the macroscopic temperature close to the ablation threshold (>44–45 °C), particularly at 37 °C. In contrast, at 4 °C, the temperature increase was insufficient to reach the required threshold, but it was enough to sensitize the cells and alter their metabolism.[73]

In the case of Balb/3T3 cells treated with GNR-H, they remained largely viable (>80%) across all temperatures and under the irradiation conditions (Fig. S2H). This is consistent

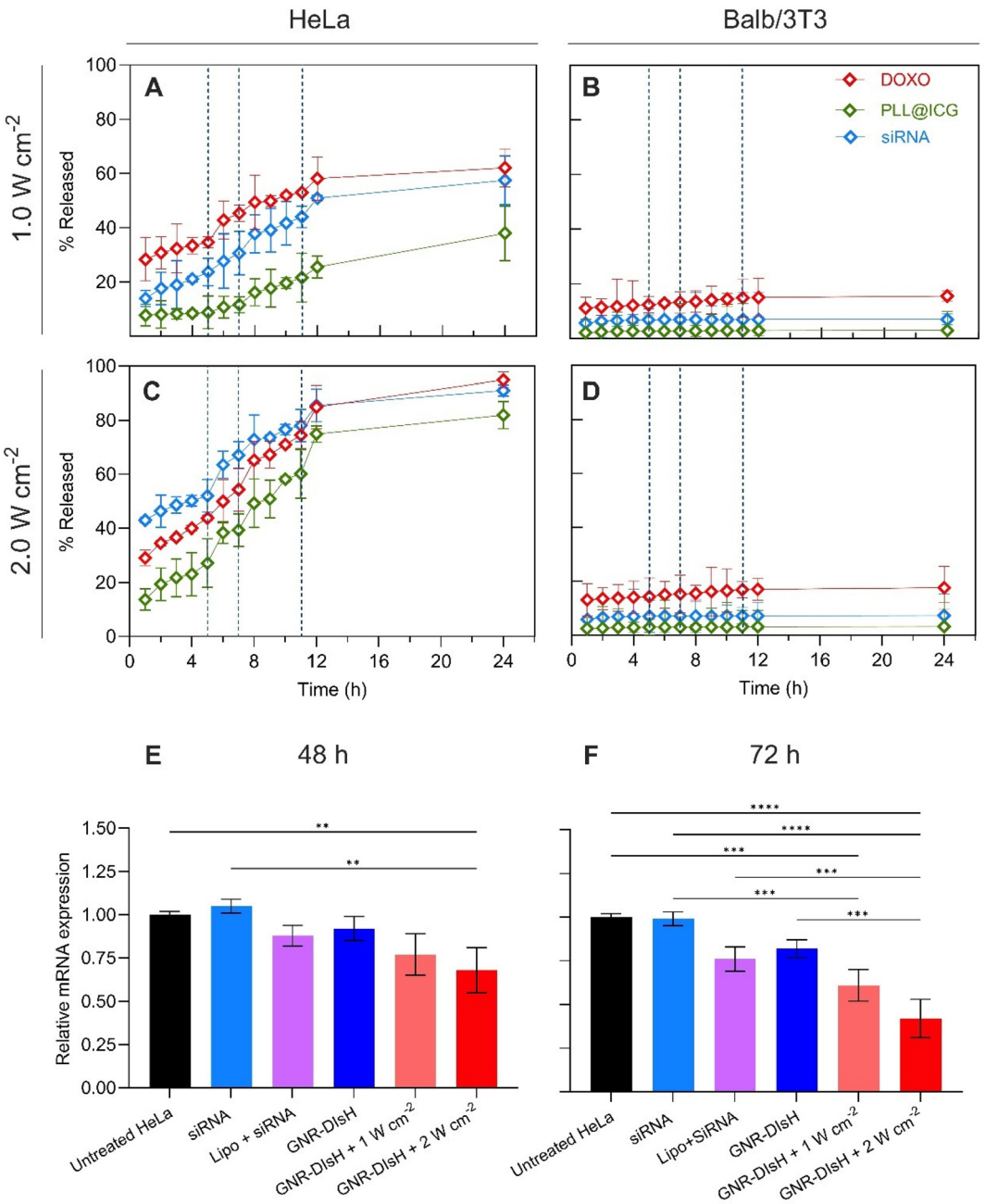


**Fig. 7** Intracellular release profiles of DOXO, PLL@ICG and siRNA from GNR-DIsH in (A and C) HeLa and (B and D) Balb/3T3 cells irradiated at (A and B) 1.0 and (B and D) 2.0 W $cm^{-2}$ after 5, 7 and 11 h of incubation (dashed lines). Relative expression of PD-L1 mRNA obtained by qRT-PCR after (E) 48 and (F) 72 h of incubation and irradiation with 1.0 and 2.0 W $cm^{-2}$ laser power densities for 5 min. Relative mRNA expression is reported as mean ± SD; $n = 3$; * $p < 0.05$, ** $p < 0.01$, *** $p < 0.001$, **** $p < 0.0001$.

with the low levels of internalization observed in this cell line, thus confirming the critical role of active targeting to achieve optimal cytotoxic effects.

Surprisingly, and despite the photothermal effect that the designed nanoplatform induced, GNR-DIsH primarily triggered cell death in HeLa cells through apoptosis, with late-apoptosis being more prominent at higher NIR light power densities (2.0 W $cm^{-2}$) and increased medium temperatures (Fig. 8A and S3). This suggests that the therapeutic activities of DOXO (early apoptosis), and ICG-mediated ROS production (late apoptosis) predominated over the plasmonic photothermal effect (necrosis). As a result, the apoptotic pathway was favored, with necrosis being the cause of a minimal 2–3% of total cell death, agreeing with the findings of previous reports.[74,75]

In contrast, for Balb/3T3 cells the levels of necrosis and apoptosis remained below 10–20% in good agreement with cytotoxicity data and exhibited a very low dependence on the

 

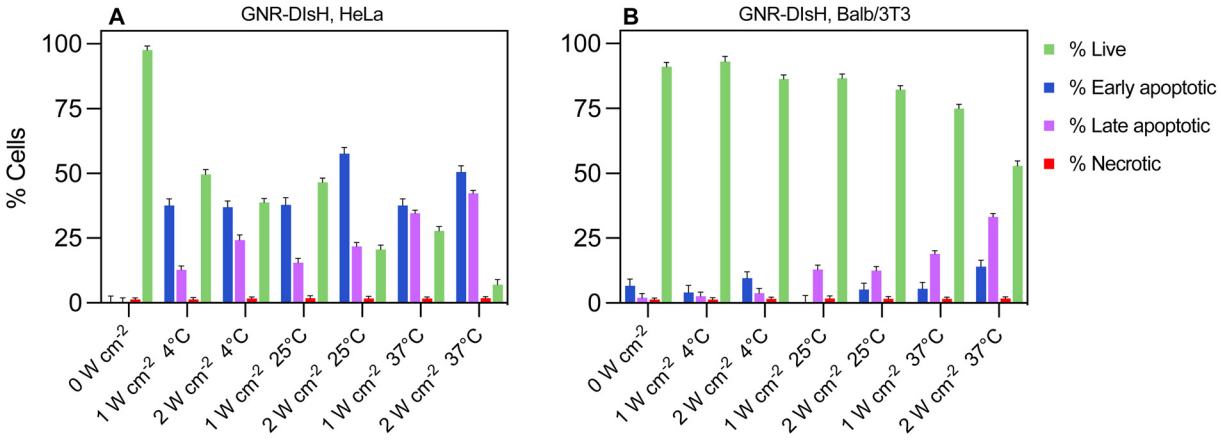


**Fig. 8** Evaluation of cell death mechanism after administration of GNR-H and GNR-DIsH, after 48 h of incubation in (A) HeLa cells and (B) Balb/3T3 cell, and irradiated with 1.0 or 2.0 W $cm^{-2}$ for 5 min at 4, 25, or 37 °C.

irradiation temperature or power density level. Only at 37 °C and 2.0 W $cm^{-2}$ did the levels of apoptosis increase in a significant way (Fig. 8B). This behavior aligned with the previously discussed poor internalization of the designed gold-based nanoplatform in this cell line.

The identification of the cell death mechanism induced by therapeutic nanoplatforms is a typically overlooked but crucial study, since it has a pronounced effect on the immune response against the tumor during post-treatment stages.[76] For example, apoptotic bodies are known to be more effective than necrotic cells in stimulating the generation of cytotoxic CD8+ T lymphocytes and provide a rich source of tumor antigens for dendritic cell processing, effectively acting as cellular tumor vaccines.[77] In contrast, necrotic cells release damage-associated molecular patterns (DAMPs) that act as signals to recruit macrophages and dendritic cells. Therefore, the combined therapy with DOXO, PDT, and PTT here proposed may contribute to reprogram the tumor microenvironment to a more immune-activated state, paving the path for a potent antitumoral immune response.[78] Moreover, the silencing of PD-L1 through the efficient transfection and release of siRNA sensitizes the surviving cancer cells to the recognition and destruction by CD8+ T lymphocytes.

In summary, the enhanced antitumor activity of our nanoplatform results from a multistep and synergistic mechanism of action. Following passive accumulation at the tumor site *via* the EPR effect and active targeting through interactions between HA and CD44, intracellular delivery is expected to be achieved. NIR-triggered irradiation promotes endosomal escape and the rapid release of bioactive agents. The combined effects of PD-L1 silencing, photothermal and photodynamic damage, and DOXO-induced cytotoxicity converge to amplify therapeutic efficacy.

Cancer heterogeneity is one of the major reasons for the failure of current therapies, not only across different patients but also, as recent studies have pointed out, due to the diversity of cellular phenotypes found within a single tumor.[79] Tumors often contain cells with diverse genetic profiles, making them less likely to respond uniformly to a single treatment. Therefore, the combination of multiple therapies and their controlled application in a rational manner could help to mitigate the development of long-term resistance and more effectively eradicate resistant and relapsing cancer cells.

## 4. Conclusion

The designed GNR-DIsH nanoplatform, functionalized through a layer-by-layer method, has been evaluated as a promising tool for the multimodal therapy of tumors. By means of surface engineering, GNR-DIsH exhibited excellent colloidal stability in various biological environments, coupled with the capability to release bioactive agents in a controlled manner through both internal and external triggers. In addition, through the integration of bioactive agents with diverse mechanisms of action, such as DOXO, ICG, and PD-L1 siRNA, the nanoplatform not only generates ROS and inhibits PD-L1 but also exerts chemotherapeutic effects, increasing the likelihood of successful therapy. The overexpression of CD44 receptors in HeLa cells facilitated the internalization of GNR-DIsH and the subsequent intracellular release of therapeutic agents, leading to a significant inhibition of cell proliferation. Through the synergistic actions of PDT, PTT, chemotherapy, and gene silencing, this nanoplatform offers a promising approach for inducing tumor cell apoptosis. Overall, these findings emphasize the potential of the designed hybrid plasmonic nanoplatform as a robust and efficient multimodal therapeutic system that can be controlled through variation of the environmental conditions and/or external stimuli.

## Author contributions

Lilia Arellano: writing – original draft, conceptualization, visualization, methodology, investigation, formal analysis, data curation. Eva Villar-Álvarez: writing – original draft, method-

ology, formal analysis, investigation, conceptualization. Adriana Cambón: writing – review & editing, methodology, supervision, data curation, validation, investigation. Alba Costa-Santos: Writing – review & editing, investigation, methodology, formal analysis. Óscar Abelenda: writing – review & editing, investigation, methodology, data curation. Alberto Pardo: writing – review & editing, visualization, investigation, validation, formal analysis, project administration. Antonio Topete: writing – review & editing, visualization, investigation, validation, formal analysis, project administration. Silvia Barbosa: writing – review & editing, writing – original draft, visualization, supervision, methodology, investigation, funding acquisition, formal analysis, data curation, conceptualization. Pablo Taboada: writing – review & editing, writing – original draft, visualization, supervision, project administration, methodology, investigation, funding acquisition, formal analysis, data curation, conceptualization.

## Conflicts of interest

The authors declare that they have no competing financial interests or personal relationships that could have appeared to influence the work reported in this paper.

## Data availability

The data that support the findings of this study are available from the corresponding author, upon reasonable request.

Detailed experimental procedures, additional physicochemical characterization, and complementary *in vitro* assays (fluorescence microscopy, ROS generation, and flow cytometry) supporting this work are provided in the Supplementary information (SI). See DOI: https://doi.org/10.1039/d5nr02667a.

## Acknowledgements

The authors thank Agencia Estatal de Investigación (AEI) for funding through projects PID2022-142682OB-I00, PCI2022-134981-2 and PID2023-152062OA-I00; and Xunta de Galicia for project ED431C 2022/28. European Regional Development Funds are also acknowledged. A. P. thanks Xunta de Galicia for grant ED481B2019/025. A. T. is thankful for the "Ramón y Cajal" fellowship RYC2023-045732-I funded by MICIU/AEI/10.13039/501100011033 and by ESF+.

## References

1 H. Sung, J. Ferlay, R. L. Siegel, M. Laversanne, I. Soerjomataram, A. Jemal and F. Bray, *CA Cancer J. Clin.*, 2021, **71**, 209–249.
2 N. Vasan, J. Baselga and D. M. Hyman, *Nature*, 2019, **575**, 299–309.
3 R. Juthani, S. Punatar and I. Mittra, *BJC Rep.*, 2024, **2**, 41.
4 D. J. Irvine and E. L. Dane, *Nat. Rev. Immunol.*, 2020, **20**, 321–334.
5 A. D. Waldman, J. M. Fritz and M. J. Lenardo, *Nat. Rev. Immunol.*, 2020, **20**, 651–668.
6 N. E. Kushlinskii, O. V. Kovaleva, A. N. Gratchev, A. A. Alferov, Y. B. Kuzmin, N. Y. Sokolov, D. A. Tsekatunov, I. B. Ryzhavskaya, I. N. Kuznetsov, D. N. Kushlinskii, Z. Z. Mamedli and I. S. Stilidi, *Biomedicines*, 2025, **13**, 500.
7 Y. Iwai, M. Ishida, Y. Tanaka, T. Okazaki, T. Honjo and N. Minato, *Proc. Natl. Acad. Sci. U. S. A.*, 2002, **99**, 12293–12297.
8 M. Soltani, M. Ghanadian, B. Ghezelbash, A. Shokouhi, A. A. Zamyatnin, A. V. Bazhin and M. Ganjalikhani-Hakemi, *BMC Cancer*, 2023, **23**, 447.
9 S. Wang, J. Li, J. Xie, F. Liu, Y. Duan, Y. Wu, S. Huang, X. He, Z. Wang and X. Wu, *Oncogene*, 2018, **37**, 4164–4180.
10 H. Ghebeh, C. Lehe, E. Barhoush, K. Al-Romaih, A. Tulbah, M. Al-Alwan, S. F. Hendrayani, P. Manogaran, A. Alaiya, T. Al-Tweigeri, A. Aboussekhra and S. Dermime, *Breast Cancer Res.*, 2010, **12**, R48.
11 K. Hudson, N. Cross, N. Jordan-Mahy and R. Leyland, *Front. Immunol.*, 2020, **11**, 1–18.
12 A. Curreri, D. Sankholkar, S. Mitragotri and Z. Zhao, *Bioeng. Transl. Med.*, 2022, e10374.
13 S. M. Elbashir, J. Harborth, W. Lendeckel, A. Yalcin, K. Weber and T. Tuschl, *Nature*, 2001, **411**, 494–498.
14 Y. Wu, W. Chen, Z. P. Xu and W. Gu, *Front. Immunol.*, 2019, **10**, 1–15.
15 J. Y. Jung, H. J. Ryu, S. H. Lee, D. Y. Kim, M. J. Kim, E. J. Lee, Y. M. Ryu, S. Y. Kim, K. P. Kim, E. Y. Choi, H. J. Ahn and S. Chang, *Cells*, 2021, **10**, 2734.
16 Y. Guo, Q. Zhang, Q. Zhu, J. Gao, X. Zhu, H. Yu, Y. Li and C. Zhang, *Sci. Adv.*, 2022, **8**, eabn2941.
17 G. Yang, D. Zhou, Y. Dai, Y. Li, J. Wu, Q. Liu and X. Deng, *Thorac. Cancer*, 2022, **13**, 2941–2950.
18 M. Scherr, M. A. Morgan and M. Eder, *Curr. Med. Chem.*, 2003, **10**, 245–256.
19 Á. Artiga, I. Serrano-Sevilla, L. De Matteis, S. G. Mitchell and J. M. de la Fuente, *J. Mater. Chem. B*, 2019, **7**, 876–896.
20 S. Liao, W. Yue, S. Cai, Q. Tang, W. Lu, L. Huang, T. Qi and J. Liao, *Front. Pharmacol.*, 2021, **12**, 1–27.
21 A. Ouhtit, Z. Y. Abd Elmageed, M. E. Abdraboh, T. F. Lioe and M. H. Raj, *Am. J. Pathol.*, 2007, **171**, 2033–2039.
22 N. Montgomery, A. Hill, S. McFarlane, J. Neisen, A. O'Grady, S. Conlon, K. Jirstrom, E. W. Kay and D. J. Waugh, *Breast Cancer Res.*, 2012, **14**, R84.
23 C. de Sousa, C. Eksteen, J. Riedemann and A.-M. Engelbrecht, *Immunol. Res.*, 2024, **72**, 592–604.
24 M. Iijima, N. Okonogi, N. I. Nakajima, Y. Morokoshi, H. Kanda, T. Yamada, Y. Kobayashi, K. Banno, M. Wakatsuki, S. Yamada, T. Kamada, D. Aoki and S. Hasegawa, *J. Gynecol. Oncol.*, 2020, **31**, e19.
25 A. Gutiérrez-Hoya, O. Zerecero-Carreón, A. Valle-Mendiola, M. Moreno-Lafont, R. López-Santiago, B. Weiss-Steider and I. Soto-Cruz, *J. Immunol. Res.*, 2019, 1242979.
26 F. Xu, F. Zhang, Q. Wang, Y. Xu, S. Xu, C. Zhang and L. Wang, *BMC Immunol.*, 2021, **22**, 60.

27 R. Roy, S. Mandal, J. Chakrabarti, P. Saha and C. K. Panda, *Mol. Cell. Biochem.*, 2021, **476**, 3701–3709.
28 P. Kogerman, M. S. Sy and L. A. Culp, *J. Cell. Physiol.*, 1996, **169**, 341–349.
29 L. G. Arellano, E. M. Villar-Alvarez, B. Velasco, V. Domínguez-Arca, G. Prieto, A. Cambón, S. Barbosa and P. Taboada, *J. Mol. Liq.*, 2023, **377**, 121511.
30 B. Nikoobakht and M. A. El-Sayed, *Chem. Mater.*, 2003, **15**, 1957–1962.
31 C. Kinnear, H. Dietsch, M. J. D. Clift, C. Endes, B. Rothen-Rutishauser and A. Petri-Fink, *Angew. Chem., Int. Ed.*, 2013, **52**, 1934–1938.
32 J. Fundin and W. Brown, *Macromolecules*, 1994, **27**, 5024–5031.
33 N. S. Gjerde, A. N. Nardi, C. G. Chen, P. Di Gianvincenzo, M. D'Abramo, A. Scipioni, L. Galantini, S. E. Moya and M. Giustini, *Phys. Chem. Chem. Phys.*, 2022, **24**, 25990–25998.
34 S. Jaiswal, S. B. Dutta, D. Nayak and S. Gupta, *ACS Omega*, 2021, **6**, 34842–34849.
35 J. Pérez-Juste, I. Pastoriza-Santos, L. M. Liz-Marzán and P. Mulvaney, *Coord. Chem. Rev.*, 2005, **249**, 1870–1901.
36 C. Yu and J. Irudayaraj, *Biophys. J.*, 2007, **93**, 3684–3692.
37 B. Manocha and A. Margaritis, *J. Nanomater.*, 2010, **2010**, 780171.
38 S. E. A. Gratton, P. A. Ropp, P. D. Pohlhaus, J. C. Luft, V. J. Madden, M. E. Napier and J. M. DeSimone, *Proc. Natl. Acad. Sci. U. S. A.*, 2008, **105**, 11613–11618.
39 Z. Gao, X. Liu, Y. Wang, G. Deng, F. Zhou, Q. Wang, L. Zhang and J. Lu, *Dalton Trans.*, 2016, **45**, 19519–19528.
40 L. Jiang, X. Li, L. Liu and Q. Zhang, *Int. J. Nanomed.*, 2013, **8**, 1825–1834.
41 J. Chen, X. Li, X. Zhao, Q. Wu, H. Zhu, Z. Mao and C. Gao, *Bioact. Mater.*, 2018, **3**, 347–354.
42 N. T. H. Lien, A. D. Phan, B. T. V. Khanh, N. T. Thuy, N. T. Nghia, H. T. M. Nhung, T. H. Nhung, D. Q. Hoa, V. Duong and N. M. Hue, *ACS Omega*, 2020, **5**, 20231–20237.
43 S. K. Maji, S. Yu, E. Choi, J. W. Lim, D. Jang, G.-y. Kim, S. Kim, H. Lee and D. H. Kim, *ACS Omega*, 2022, **7**, 15186–15199.
44 R. Venkatesan, A. Pichaimani, K. Hari, P. K. Balasubramanian, J. Kulandaivel and K. Premkumar, *J. Mater. Chem. B*, 2013, **1**, 1010–1018.
45 U. A. Awan, A. Raza, S. Ali, R. F. Saeed and N. Akhtar, *Beilstein J. Nanotechnol.*, 2021, **12**, 295–303.
46 L.-S. Li, B. Ren, X. Yang, Z.-C. Cai, X.-J. Zhao and M.-X. Zhao, *Pharmaceuticals*, 2021, **14**, 1–13.
47 R. Venkatesan, A. Pichaimani, K. Hari, P. K. Balasubramanian, J. Kulandaivel and K. Premkumar, *J. Mater. Chem. B*, 2013, **1**, 1010–1018.
48 B. Gong, Y. Shen, H. Li, X. Li, X. Huan, J. Zhou, Y. Chen, J. Wu and W. Li, *J. Nanobiotechnol.*, 2021, **19**, 41.
49 W.-S. Kuo, Y.-T. Chang, K.-C. Cho, K.-C. Chiu, C.-H. Lien, C.-S. Yeh and S.-J. Chen, *Biomaterials*, 2012, **33**, 3270–3278.
50 W.-S. Kuo, C.-N. Chang, Y.-T. Chang, M.-H. Yang, Y.-H. Chien, S.-J. Chen and C.-S. Yeh, *Angew. Chem.*, 2010, **122**, 2771–2775.
51 T. Luo, X. Qian, Z. Lu, Y. Shi, Z. Yao, X. Chai and Q. Ren, *J. Biomed. Nanotechnol.*, 2015, **11**, 600–612.
52 R. Sun, Y. Wang, Q. Sun, Y. Su, J. Zhang, D. Liu, R. Huo, Y. Tian, M. Baldan, S. Zhang and C. Cui, *Mol. Pharm.*, 2024, **21**, 5455–5468.
53 K. Guo, S. Ren, H. Zhang, Y. Cao, Y. Zhao, Y. Wang, W. Qiu, Y. Tian, L. Song and Z. Wang, *ACS Appl. Mater. Interfaces*, 2023, **15**, 25285–25299.
54 R. Fan, C. Chen, J. Hu, M. Mu, D. Chuan, Z. Chen, G. Guo and J. Xu, *Acta Biomater.*, 2023, **159**, 324–337.
55 B. Lu, D. Luo, A. Zhao, H. Wang, Y. Zhao, M. F. Maitz, P. Yang and N. Huang, *Prog. Org. Coat.*, 2019, **135**, 240–247.
56 A. L. Villela Zumaya, R. Mincheva, J.-M. Raquez and F. Hassouna, *Polymers*, 2022, **14**, 1188.
57 S. Misra, V. C. Hascall, R. R. Markwald and S. Ghatak, *Front. Immunol.*, 2015, **6**, 1–31.
58 L. Ceriotti, A. Kob, S. Drechsler, J. Ponti, E. Thedinga, P. Colpo, R. Ehret and F. Rossi, *Anal. Biochem.*, 2007, **371**, 92–104.
59 H. Chang Kang and Y. H. Bae, *Biomaterials*, 2011, **32**, 4914–4924.
60 Y.-S. Chen, S. J. Yoon, W. Frey, M. Dockery and S. Emelianov, *Nat. Commun.*, 2017, **8**, 15782.
61 M. K. Yu, J. Park and S. Jon, *Theranostics*, 2012, **2**, 3–44.
62 G. C. Thurner and P. Debbage, *Histochem. Cell Biol.*, 2018, **150**, 733–794.
63 Z. S. Silva, Jr., S. K. Bussadori, K. P. S. Fernandes, Y.-Y. Huang and M. R. Hamblin, *Biosci. Rep.*, 2015, **35**, e00265.
64 M. M. Kim and A. Darafsheh, *Photochem. Photobiol.*, 2020, **96**, 280–294.
65 N. Escareño, A. A. Villanueva-Briseño, A. Topete and A. Daneri-Navarro, in *Nanomaterials for Photodynamic Therapy*, ed. P. Kesharwani, Woodhead Publishing, 2023, pp. 459–488, DOI: 10.1016/B978-0-323-85595-2.00001-3.
66 D. L. Li, Z. V. Wang, G. Ding, W. Tan, X. Luo, A. Criollo, M. Xie, N. Jiang, H. May, V. Kyrychenko, J. W. Schneider, T. G. Gillette and J. A. Hill, *Circulation*, 2016, **133**, 1668–1687.
67 R. P. Hickerson, A. V. Vlassov, Q. Wang, D. Leake, H. Ilves, E. Gonzalez-Gonzalez, C. H. Contag, B. H. Johnston and R. L. Kaspar, *Oligonucleotides*, 2008, **18**, 345–354.
68 A. Sharma, S. Özayral, J. S. Caserto, R. ten Cate, N. M. Anders, J. D. Barnett, S. K. Kandala, E. Henderson, J. Stewart, E. Liapi, M. A. Rudek, N. A. P. Franken, A. L. Oei, P. Korangath, F. Bunz and R. Ivkov, *Int. J. Hyperthermia*, 2019, **36**, 711–719.
69 H. Mizobuchi, W. Fujii, K. Ishizuka, Y. Wang, S. Watanabe, C. Sanjoba, Y. Matsumoto and Y. Goto, *Immunol. Lett.*, 2018, **194**, 13–20.
70 V. A. Patel, A. Longacre, K. Hsiao, H. Fan, F. Meng, J. E. Mitchell, J. Rauch, D. S. Ucker and J. S. Levine, *J. Biol. Chem.*, 2006, **281**, 4663–4670.

71 C. Shirata, J. Kaneko, Y. Inagaki, T. Kokudo, M. Sato, S. Kiritani, N. Akamatsu, J. Arita, Y. Sakamoto, K. Hasegawa and N. Kokudo, *Sci. Rep.*, 2017, **7**, 13958.
72 S. Wang, E. A. Konorev, S. Kotamraju, J. Joseph, S. Kalivendi and B. Kalyanaraman, *J. Biol. Chem.*, 2004, **279**, 25535–25543.
73 A. T. Haine and T. Niidome, *Chem. Pharm. Bull.*, 2017, **65**, 625–628.
74 C. K. Sen, *Wound Repair Regener.*, 2003, **11**, 431–438.
75 T. J. Guzik, R. Korbut and T. Adamek-Guzik, *J. Physiol. Pharmacol.*, 2003, **54**, 469–487.
76 C. Ma, Z. Cheng, H. Tan, Y. Wang, S. Sun, M. Zhang and J. Wang, *Front. Immunol.*, 2024, **15**, 1–31.
77 K. Plaetzer, T. Kiesslich, T. Verwanger and B. Krammer, *Med. Laser Appl.*, 2003, **18**, 7–19.
78 J. Zhang, S. Wang, D. Zhang, X. He, X. Wang, H. Han and Y. Qin, *Front. Immunol.*, 2023, **14**, 1230893.
79 J. Klughammer, D. L. Abravanel, Å. Segerstolpe, T. R. Blosser, Y. Goltsev, Y. Cui, D. R. Goodwin, A. Sinha, O. Ashenberg, M. Slyper, S. Vigneau, J. Jané-Valbuena, S. Alon, C. Caraccio, J. Chen, O. Cohen, N. Cullen, L. K. DelloStritto, D. Dionne, J. Files, A. Frangieh, K. Helvie, M. E. Hughes, S. Inga, A. Kanodia, A. Lako, C. MacKichan, S. Mages, N. Moriel, E. Murray, S. Napolitano, K. Nguyen, M. Nitzan, R. Ortiz, M. Patel, K. L. Pfaff, C. B. M. Porter, A. Rotem, S. Strauss, R. Strasser, A. R. Thorner, M. Turner, I. Wakiro, J. Waldman, J. Wu, J. Gómez Tejeda Zañudo, D. Zhang, N. U. Lin, S. M. Tolaney, E. P. Winer, E. S. Boyden, F. Chen, G. P. Nolan, S. J. Rodig, X. Zhuang, O. Rozenblatt-Rosen, B. E. Johnson, A. Regev and N. Wagle, *Nat. Med.*, 2024, **30**, 3236–3249.